

## Rainfall-induced slope collapse with coupled material point method

Wang, B.; Vardon, P. J.; Hicks, M. A.

**DOI**

[10.1016/j.enggeo.2018.02.007](https://doi.org/10.1016/j.enggeo.2018.02.007)

**Publication date**

2018

**Document Version**

Final published version

**Published in**

Engineering Geology

**Citation (APA)**

Wang, B., Vardon, P. J., & Hicks, M. A. (2018). Rainfall-induced slope collapse with coupled material point method. *Engineering Geology*, 239, 1-12. <https://doi.org/10.1016/j.enggeo.2018.02.007>

**Important note**

To cite this publication, please use the final published version (if applicable).  
Please check the document version above.

**Copyright**

Other than for strictly personal use, it is not permitted to download, forward or distribute the text or part of it, without the consent of the author(s) and/or copyright holder(s), unless the work is under an open content license such as Creative Commons.

**Takedown policy**

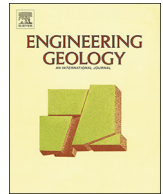
Please contact us and provide details if you believe this document breaches copyrights.  
We will remove access to the work immediately and investigate your claim.

***Green Open Access added to TU Delft Institutional Repository***

***'You share, we take care!' – Taverne project***

**<https://www.openaccess.nl/en/you-share-we-take-care>**

Otherwise as indicated in the copyright section: the publisher is the copyright holder of this work and the author uses the Dutch legislation to make this work public.



# Rainfall-induced slope collapse with coupled material point method

B. Wang<sup>a,b</sup>, P.J. Vardon<sup>a</sup>, M.A. Hicks<sup>a,\*</sup>

<sup>a</sup> Geo-Engineering Section, Faculty of Civil Engineering and Geosciences, Delft University of Technology, Delft, The Netherlands

<sup>b</sup> State Key Laboratory of Geomechanics and Geotechnical Engineering, Institute of Rock and Soil Mechanics, Chinese Academy of Sciences, Wuhan, China



## ARTICLE INFO

### Keywords:

Large deformations  
Material point method  
Rainfall-induced failure  
Slope stability  
Unsaturated soils

## ABSTRACT

Rainfall-induced slope failures are a major category of slope failure, with incidents likely to increase with the predicted escalation of extreme rainfall events. Traditional numerical methods such as the finite element method are often restricted in their applicability to small deformation analyses. Therefore, incomplete descriptions of the failure mechanism and failure consequence may be obtained, due to the evolving deformations and progressive failure being ignored. A one-point, two-phase material point method (MPM) formulation is proposed to consider the influence of rainfall on slope failure. Due to the characteristics of MPM in capturing the large deformations, the complete failure process, from initiation to failure, of a slope subjected to rainfall infiltration is presented. The soil behaviour is described by a Mohr–Coulomb strain-softening model based on Bishop's effective stress. The two-phase analysis shows that the rainfall-affected slope is initially stable, until the soil shear strength reduces due to the reduction of suction in the slope starting from the surface, leading to a superficial failure mode, which in turn leads to a complete slope failure. Friction angle and residual cohesion are shown to play important roles in the development of the slope failure.

## 1. Introduction

Rainfall is considered to be a major factor triggering slope failures around the world. It is recognized that rainfall infiltration results in a rise of the groundwater table and an increase of the pore water pressure, or, in the decrease of matric suction in unsaturated soils (Cai and Ugai, 2004), which in turn causes a reduction in effective normal stress and thereby soil strength along the potential failure path (Brand, 1981; Fredlund and Rahardjo, 1993). Extreme rainfall events are also likely to increase in frequency causing an increase in slope failures (Vardon, 2015).

Numerous analyses have been conducted to investigate the effects of rainfall infiltration on slope stability. Dai and Lee (2001) investigated the relationship between rainfall and the occurrence of landslides, and indicated that the rainfall in the preceding 12 h is most important in predicting the number of slides. Results from Tsaparas et al. (2002) showed that, for the same rainfall, the higher the value of the saturated coefficient of permeability, the smaller the factor of safety of the slope will be, due to a deeper wetting front. Lin et al. (2006) compared the occurrence of landslides which occurred from 1996 to 2001 along the Choushui River in central Taiwan (after the Chi-Chi earthquake), and found that the density of rainfall-induced landslides had significantly increased. Rahardjo et al. (2007) compared the relationship between rainfall intensity and minimum factor of safety for a homogeneous slope

subjected to rainfall for 24 h, and suggested that the ratio of intensity over saturated coefficient of permeability should be used as an indicator of slope stability, rather than either of them alone being used. Borja et al. (2012) proposed a methodology for coupling physics-based continuum modelling with limit equilibrium calculations, to evaluate the factor of safety of a slope subjected to rainfall infiltration. Meanwhile, Wu et al. (2016) developed an analytical approach for rainfall infiltration (and its consequences) in an unsaturated porous medium, including an analytical solution for the factor of safety of an infinite partially saturated slope. However, these efforts have mainly been focused on the failure initiation stage, thereby providing an incomplete description of the slope failures. Cascini et al. (2009) modelled a shallow landslide of the flow-type in Southern Italy, in which the landslide behaviour was divided into two stages: failure and post-failure. The failure stage is characterized by the formation of a continuous shear band through the soil mass, with little overall movement of the soil body (Leroueil, 2001). The post-failure stage is described by the rapid generation of plastic strains and the resulting sudden acceleration of the failed soil mass (Hungri, 2003). Relatively little research has been done so far to describe the post-failure stage numerically (an exception being Pastor et al. (2004)), but such analyses can be considered particularly useful, as they contribute to the assessment of the landslide volumes and their potential for travelling long distances (Cascini et al., 2009). USGS (2004) describe several types of slope

\* Corresponding author.

E-mail address: [m.a.hicks@tudelft.nl](mailto:m.a.hicks@tudelft.nl) (M.A. Hicks).

failure. It can be seen that the post-failure behaviour ranges from retrogressive failures, where the material moves away from the initial failure in discrete slides, to flow slides where the material weakens and flows away from the failure zone.

The material point method (MPM) has proven to be a reliable tool in capturing large deformations in geotechnical analyses, since its first application to solid mechanics in 1994 (Sulsky et al., 1994, 1995). By utilising an implicit time integration scheme, an implicit material point method framework (IMPM) was proposed by Wang et al. (2016a, 2016b), and the retrogressive failure of clayey slopes, as often observed in practice, were modelled. Moreover, by combining random field theory and the material point method, the random material point method (RMPM) was proposed by Wang et al. (2016c), in which the importance of considering the effects of both large deformations and spatial variability of soil strength properties in slope stability analyses was highlighted. Other modelling methods have been proposed to tackle large deformation problems, such as the discrete element method (DEM), smoothed particle hydrodynamics (SPH), coupled Eulerian–Lagrangian (CEL) method and arbitrary Lagrangian–Eulerian (ALE) method. Soga et al. (2016) presented a review of these methods. For both DEM and SPH it is difficult to use continuum constitutive models, whereas both the CEL and ALE methods are related to FEM, but have disadvantages over MPM relating to solving advective material behaviour and mesh tangling, respectively.

More recently, efforts have been focused on the simulation of coupled hydro-mechanical processes in saturated/unsaturated soils with MPM, although this research is still in its infancy. Following the standard finite element method (FEM) procedure, two main formulations (considering dynamic analysis only) can be identified, based on whether or not to include the inertial terms. The full set of governing equations used in describing the dynamic motion is the  $v$ – $w$  formulation, where the velocities or displacements of the solid phase and the fluid phase, e.g. water, are used as the primary variables. It can be used to represent the most general soil behaviour and is convenient for the finite element formulation, although it results in a large number of nodal unknowns (Zienkiewicz et al., 1980). An alternative simplification is also possible, where the primary variables are the solid phase velocities or displacements and the pore pressures, i.e. the  $v$ – $p$  or  $u$ – $p$  formulation. Van Esch et al. (2011) compared the two formulations, concluding that the time step size is more restrictive and the second compression wave cannot be accurately captured when the  $v$ – $p$  formulation is applied. So far, most MPM implementations have used  $v$ – $w$  formulations (Zhang et al., 2007; Abe et al., 2013; Jassim et al., 2013; Bandara and Soga, 2015).

Jassim et al. (2013) adopted the  $v$ – $w$  formulation while representing the solid and fluid phases by the same material point, with each phase taking a fraction of the material point domain. Following the procedure outlined by Verruijt (2009), the velocities of the fluid and solid phases were solved in sequence. The material point positions were updated based on the velocities of the solid phase, while the water velocities were simply used for the pore pressure calculation. The enhancement of volumetric strains was used to mitigate spurious pressure fields and locking problems which may arise when using low-order elements. In order to achieve a smooth stress variation, stress integration was performed on the Gauss points if at least 90% of the element area/volume was filled with material points; otherwise it was performed on the material points. This led to a violation of the mass conservation, due to the true material point volumes not being represented. Bandara and Soga (2015) derived their  $v$ – $w$  formulation based on mixture theory, with the key aspect of the formulation being that it considered two sets of material points; one for the solid phase and one for the fluid phase. Yerro et al. (2015) continued the research by Jassim et al. (2013), and proposed a one-point, three-phase (solid, liquid, gas) formulation. The velocities of the gas, fluid and solid phases were calculated sequentially, based on the momentum balance equations for the gas phase, fluid phase and mixture.

In contrast,  $v$ – $p$  or  $u$ – $p$  formulations within the MPM framework were mainly developed during an earlier period. Zhang et al. (2009) proposed a coupled MPM formulation based on a  $u$ – $p$  form of the FEM governing equations for saturated soils, where the displacements of the solid skeleton and the pore pressures were the main unknowns. A contact algorithm was also developed to simulate the interaction between saturated soils and structures, which enabled the simulation of saturated soils under contact/impact. Zabala and Alonso (2011) applied the method, coupled with a strain-softening Mohr–Coulomb elastoplastic model, to simulate the construction and failure of the Aznalcollar dam, where the rupture process was captured and well matched to actual field observations. Lim et al. (2014) modelled a spudcan foundation penetrating into a fully saturated soil, by utilising a  $v$ – $p$  formulation with MPM. To mitigate potential volumetric locking due to the linear elements of the computational grid, an alternative form of the Hu–Washizu weak form was implemented.

In this paper, a new MPM formulation for unsaturated soils has been proposed, considering two phases and a single material point. It is an effective stress-type formulation, unlike some others, and is based on the  $v$ – $w$  formulation proposed by Jassim et al. (2013) for fully saturated soils; in particular, by considering the degree of saturation within the governing equations, a simplified one-point, two-phase unsaturated formulation for dynamic MPM is derived. For simplicity, the gas phase is omitted, although it may be included in a very straight-forward way as in FEM. A B-bar shape function, for which details can be found in Hughes (1980), is included to stabilise the pore pressure, which has not previously been considered in other hydro-mechanical MPM formulations. The formulation and corresponding assumptions are briefly described first, and a simple infiltration example is analysed to validate the unsaturated formulation. Slope failure analyses are then presented, where the importance of rainfall in slope failure initiation and propagation is highlighted.

## 2. Formulation of the material point method for unsaturated soils

### 2.1. Conservation of solid mass

As for saturated soils, the solid mass conservation is described as

$$\frac{\partial(1-n)\rho_s}{\partial t} + \nabla(1-n)\rho_s \mathbf{v}_s = 0 \quad (1)$$

where  $\rho_s$  is the density of the solid grains,  $n$  is the porosity,  $t$  is time, and  $\mathbf{v}_s$  denotes the velocity of the solid particles. By neglecting the gradient of porosity, and assuming the solid particles are incompressible, Eq. (1) can be simplified as

$$\frac{\partial n}{\partial t} = (1-n)\nabla \mathbf{v}_s \quad (2)$$

### 2.2. Conservation of fluid mass

The conservation of the fluid (water) is expressed as

$$\frac{\partial nS\rho_w}{\partial t} + \nabla nS\rho_w \mathbf{v}_w = 0 \quad (3)$$

where  $\rho_w$  and  $\mathbf{v}_w$  are the density and velocity of the fluid, respectively, and  $S$  is the degree of saturation of the soil. By using the chain rule, the equation is expanded as

$$S\rho_w \frac{\partial n}{\partial t} + n\rho_w \frac{\partial S}{\partial t} + nS \frac{\partial \rho_w}{\partial t} + nS\rho_w \nabla \mathbf{v}_w + \mathbf{v}_w \nabla nS\rho_w = 0 \quad (4)$$

By substituting Eq. (2) into Eq. (4) to eliminate the material time derivative of the porosity, neglecting the spatial water density gradient, and dividing the whole equation by the water density  $\rho_w$ , the mass balance equation for water reduces to

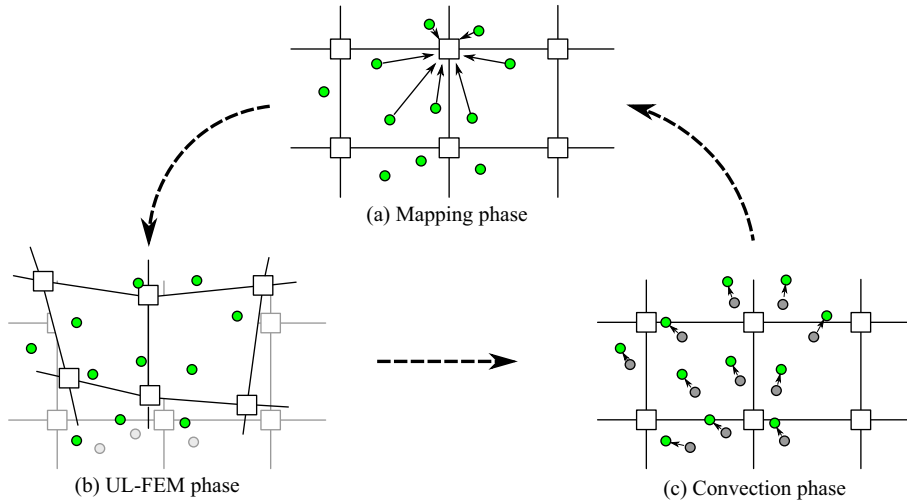


**Fig. 1.** Computational cycle of MPM. (a) A set of material points representing the material, overlaid on a background computational mesh. Material properties, constitutive models and other state information are assigned to, and stored only on, the material points. Information is transferred to the nodes of the background mesh for computational purposes. (b) The equations of motion are solved on the background mesh, utilising Updated Lagrangian FEM. (c) The state of the material points is updated, and the background mesh reset.

$$n \frac{\partial S}{\partial t} + \frac{nS}{\rho_w} \frac{\partial \rho_w}{\partial t} + nS \nabla \mathbf{v}_w + (1-n)S \nabla \mathbf{v}_s = 0 \quad (5)$$

Assuming a barotropic behaviour for the fluid, its intrinsic density variation is given by

$$\frac{1}{\rho_w} \frac{\partial \rho_w}{\partial t} = -\frac{1}{K_w} \frac{dp_w}{dt} \quad (6)$$

where  $K_w$  is the bulk modulus of water which is assumed to be constant, and  $p_w$  is the water pressure. Hence, the time derivative of the degree of saturation can be written as

$$\frac{\partial S}{\partial t} = \frac{\partial S}{\partial s} \frac{\partial s}{\partial t} = -\frac{\partial S}{\partial s} \frac{dp_w}{dt} = -\lambda \frac{dp_w}{dt} \quad (7)$$

where  $s$  is the suction, which is simply taken to be  $-p_w$  due to the gas phase being ignored in the analysis, and  $\lambda$  is an intermediate modulus equal to  $\partial S / \partial s$ . By substituting Eqs. (2), (6) and (7) into Eq. (5), after simple algebraic manipulation the water pressure can be obtained as

$$\frac{dp_w}{dt} = \left( n\lambda - n \frac{S}{K_w} \right)^{-1} (nS \nabla \mathbf{v}_w + (1-n)S \nabla \mathbf{v}_s) \quad (8)$$

### 2.3. Momentum conservation for fluid

The momentum equation for laminar fluid flow in an unsaturated soil is

$$\rho_w \mathbf{a}_w = \nabla p_w + \rho_w \mathbf{b} - \frac{nS\mu_w}{k} (\mathbf{v}_w - \mathbf{v}_s) \quad (9)$$

where  $\mathbf{a}_w$  is the fluid acceleration,  $\mathbf{b}$  is the body force,  $k$  is the soil permeability and  $\mu_w$  is the water viscosity. The last term in Eq. (9) refers to the fluid–solid interaction term, which is proportional to the fluid velocity relative to the solid velocity. It is assumed that the flow remains laminar here, even during large deformations, as it is fluid flow through the material that is considered. Other hydro-mechanical failure mechanisms, e.g. erosion or overtopping, may involve a fast flowing free fluid phase or turbulent flow within the soil, for which a formulation including non-laminar flow would be required (e.g. Kularathna and Soga, 2017; Maljaars et al., 2017).

### 2.4. Momentum conservation for mixture

The momentum conservation for the mixture is

$$(1-n)\rho_s \mathbf{a}_s + nS\rho_w \mathbf{a}_w = \nabla \cdot \boldsymbol{\sigma} + (1-n)\rho_s \mathbf{b} + nS\rho_w \mathbf{b} \quad (10)$$

where  $\mathbf{a}_s$  is the solid acceleration, and Bishop's effective stress is utilised in the calculation of the total stress  $\boldsymbol{\sigma}$ , i.e.

$$\boldsymbol{\sigma}' = \boldsymbol{\sigma} - \mathbf{m}(\chi p_w) \quad (11)$$

where  $\chi$  is an effective stress parameter called the matric suction coefficient and varies from 0 to 1 covering the range from dry to fully saturated conditions. For convenience,  $\chi$  is simplified to equal the degree of saturation,  $S$ , in the following calculations.  $\mathbf{m}$  is the unit vector  $[1101]^T$  for 2D plane strain analysis. As already stated, gas pressure is omitted for simplicity. It is noted that Bishop's effective stress in this form reduces to effective stress at full saturation, thereby forming a smooth transition between the unsaturated and saturated stress conditions.

### 2.5. Material point method

To solve the momentum balance equations, i.e. Eqs. (9) and (10), they must be spatially discretised. The space discretisation is conducted by utilising MPM, in which there are two levels of discretisation represented by a collection of material points and a fixed background mesh. The continuum is represented by the material points, with each point occupying a corresponding volume, though not necessarily defined as an explicit shape in the traditional MPM. The material properties, constitutive models and other state information are assigned to the material points. Under external force/traction loading, the material points are allowed to move freely through the background mesh. The background mesh is only for the computation and does not store any information.

An illustration of a computational cycle in the material point method is shown in Fig. 1, where three computation phases are identified; i.e. the mapping, updated Lagrangian FEM, and convective phases. Details of the space discretisation of the governing equations, as well as of the mapping of information back and fore between the background mesh and material points, can be found in Chen and Brannon (2002) and Yerro et al. (2015).

### 2.6. Numerical procedures within a computational cycle

A discretisation in time is necessary for solving the momentum balance equations and, for this purpose, an explicit time integration scheme has been chosen. The two-phase coupled MPM algorithm is summarised as follows:

- 1) Initialization of all the variables on the nodes.
- 2) Acceleration of the water phase is solved using Eq. (9).

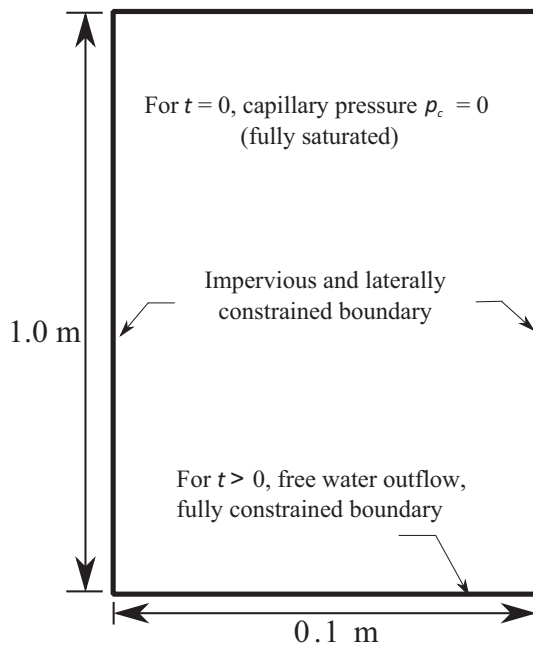


Fig. 2. Numerical model of Liakopoulos' (1964) test problem (not to scale).

- 3) Acceleration of the solid phase is obtained using Eq. (10).
- 4) The velocities of the two phases on the nodes are updated using the explicit forward Euler method.
- 5) The velocities of the two phases on the material points are updated, and then the positions of the material points are updated based on the calculated velocities of the solid particles.
- 6) The velocities on the nodes are updated by mapping back from the material points, and then the stresses and water pressures on the material points are calculated.
- 7) The background mesh is reset, and the next computational cycle is initiated.

### 2.7. Infiltration example

For validating the coupled MPM code for unsaturated soils, the laboratory test by Liakopoulos (1964) has been analysed. The experiment was performed on a column of Del Monte sand, which was initially fully saturated by adding water from the top continuously. The water supply was stopped at the start of the experiment. The two side walls were impermeable to water, while the water was able to freely drain from the bottom, and tensiometers located along the column height were used to measure the moisture tension during the desaturation due to gravity. A schematic diagram of Liakopoulos' test is shown in Fig. 2, where the initial and boundary conditions are defined.

The material properties are given in Table 1. The relationships between saturation–capillary pressure and relative

permeability–saturation, valid for saturation  $S > 0.91$ , take the following forms (Lewis and Schrefler, 1998):

$$S = 1.0 - 1.9722 \times 10^{11} p_w^{2.4279} \tag{12}$$

$$k_{rel} = 1.0 - 2.207(1.0 - S)^{1.0121} \tag{13}$$

where  $k_{rel}$  is the relative permeability, which is the ratio between the actual permeability and the permeability at full saturation.

For the analysis, the column of sand was divided into 10 4-node quadrilateral elements of size 0.1 m × 0.1 m, with each element initially containing 4 material points, thereby giving 40 material points in total for the column. The time step size was set to  $5.0 \times 10^{-6}$  s. The results of the simulation at different times, i.e. the water saturation, vertical displacement and capillary pressure, are shown in Fig. 3. Small strain analysis was utilised in the calculation due to the small vertical displacements. A gradually decreasing outflow rate is observed, due to the reducing rate of change of pore pressure at the top of the specimen. The reasonable agreement between the computed and experimental results demonstrates the applicability of the model for unsaturated soils.

### 3. Investigation of rainfall-induced slope failure

The rainfall-induced failure process of a long slope is presented in this section. The general characteristics of the slope are described first. Then, illustrative computations of the retrogressive failure process as water infiltrates into the slope are presented. These are followed by comparisons with a total stress analysis, to emphasize the important role of rainfall in the slope failure initiation and subsequent failure propagation. The influences of soil friction angle and residual cohesion on the slope failure mechanism are discussed last.

#### 3.1. Characteristics of long slope on an inclined base

Fig. 4 shows the slope geometry that comprises a 5 m deep soil layer, a main slope inclined at 20° and, to avoid boundary effects, a horizontal section at the top of the slope. Towards the bottom of the slope, a smaller cut slope has been made to a depth of 4.0 m, at an inclination of 45° to the main slope surface (i.e. at 65° to the horizontal). The horizontal section is 15 m long, whereas the slope is over 40 m long (along the line of the slope). The boundary conditions include rollers at both sides of the domain, preventing horizontal displacement, and a fully fixed bottom boundary to simulate a perfectly rough interface with bedrock below. The model is discretised using 842, 4-node quadrilateral elements, with initially 4 material points per element located at the Gauss point locations, giving a total of 3368 material points representing the slope. The simulation stops when failure is fully developed in the slope, i.e. when the soil has reached the static condition, defined here as the accelerations at all points being negligible.

A suction-dependent Mohr–Coulomb model, i.e. using Bishop's effective stress, has been adopted to describe the soil response, in which the cohesion is assumed to decrease proportionally with the equivalent plastic shear strain invariant until reaching the residual value, and the friction and dilation angles remain constant. Due to the choice of using Bishop's effective stress, the shear strength reduction due to the reduction of suction is automatically included in the model; utilising two stress state parameters, e.g. net stress and suction, requires additional parameterisation to incorporate this behaviour. The shear strength reduction based on shear strain in this model is material specific and due to the breakup of soil structure; for example, as in the breaking of particle cementation in sand and as has been illustrated in the simulation of sensitive clay slopes (Wang et al., 2016b). Fig. 5 shows a sketch of the model, where the stress–strain relationship in the softening stage is assumed to be linear and given by.

Table 1

Material properties for analysis of Liakopoulos' test (Lewis and Schrefler, 1998).

Parameters	Values
Young's modulus (kPa)	$1.3 \times 10^3$
Poisson's ratio	0.4
Solid grain density (kg/m <sup>3</sup> )	$2.0 \times 10^3$
Fluid density (kg/m <sup>3</sup> )	$1.0 \times 10^3$
Porosity	0.2975
Intrinsic permeability (m <sup>2</sup> )	$1.0 \times 10^{-13}$
Fluid viscosity (Pa·s)	$1.0 \times 10^{-3}$
Gravitational acceleration (m/s <sup>2</sup> )	9.806

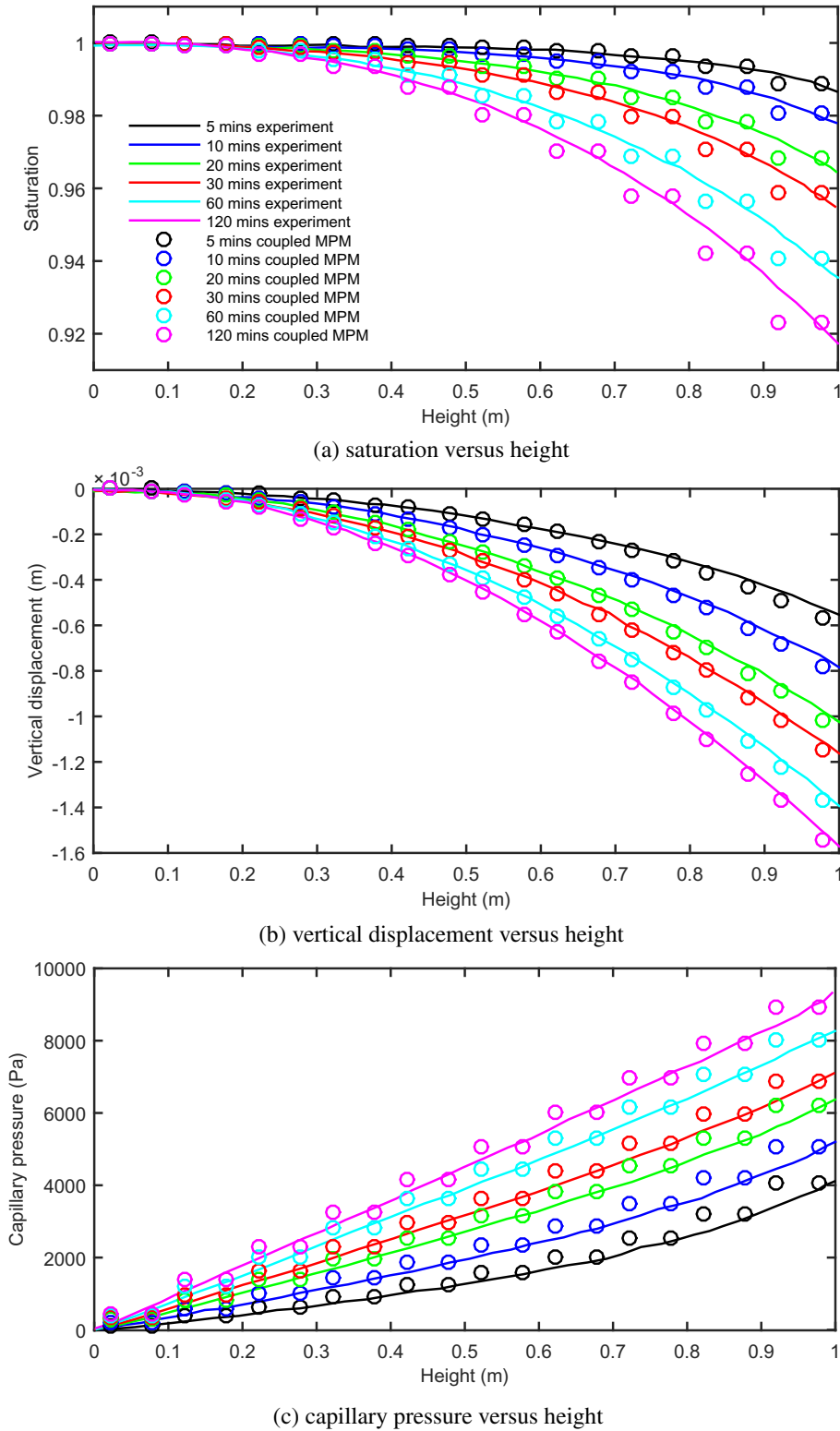


Fig. 3. Comparisons between MPM and experimental results.

$$c(\bar{\epsilon}_p) = c_0 + H \cdot \bar{\epsilon}_p ; \bar{\epsilon}_p < \bar{\epsilon}_{pr} \quad (14)$$

$$c(\bar{\epsilon}_p) = c_r ; \bar{\epsilon}_p \geq \bar{\epsilon}_{pr} \quad (15)$$

where  $c_0$  is the initial cohesion,  $c_r$  is the residual cohesion,  $\bar{\epsilon}_p$  is the accumulated plastic shear strain invariant,  $\bar{\epsilon}_{pr}$  is the plastic shear strain invariant at the onset of the residual strength and  $H$  is the softening modulus (which is taken to be negative). A softening modulus of

–250.0 kPa has been used in the following analyses.

The van Genuchten (1980) model has been used to describe the relationship between the degree of saturation,  $S$ , the permeability of the soil with respect to the fluid phase,  $k$ , and the pore water pressure  $p_w$ . The so-called effective degree of saturation  $S_e$  is thus given by.

$$S_e(s) = (1 + (\alpha_{sw} s)^{n_s})^{-(1-1/n_s)} ; s \geq 0 \quad (16a)$$

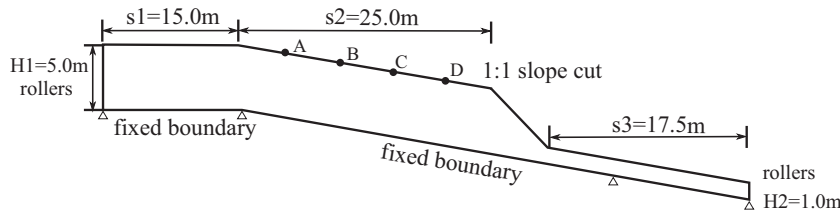


Fig. 4. Initial geometry of the slope (not to scale).

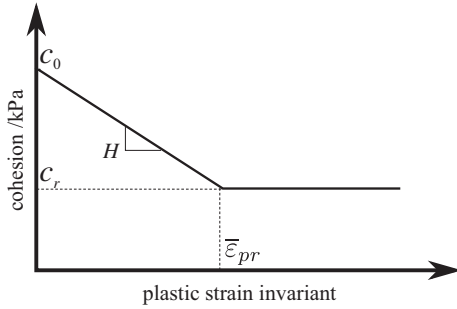


Fig. 5. Sketch of cohesion-softening model.

Table 2  
Material properties for slope analysis.

Parameters	Values
Young's modulus (kPa)	$1.0 \times 10^4$
Poisson's ratio	0.33
Solid grain density ( $\text{kg/m}^3$ )	$2.7 \times 10^3$
Fluid density ( $\text{kg/m}^3$ )	$1.0 \times 10^3$
Porosity	0.3
Intrinsic permeability ( $\text{m}^2$ )	$4.5 \times 10^{-9}$
Fluid viscosity (Pa.s)	$1.0 \times 10^{-3}$
Peak cohesion (kPa)	20.0
Residual cohesion (kPa)	0.1
Friction angle ( $^\circ$ )	20.0
Dilation angle ( $^\circ$ )	0.1

$$S_e(s) = S_{sat} ; s < 0 \quad (16b)$$

where  $\alpha_{sw}$  and  $n_s$  are fitting parameters, and the effective degree of saturation is defined as

$$S_e = \frac{S - S_{res}}{S_{sat} - S_{res}} \quad (17)$$

where  $S_{sat}$  and  $S_{res}$  are the degree of saturation at full saturation and the residual degree of saturation under very dry conditions, and were respectively taken as 1.0 and 0.23 in the following analyses.

It is common to express the actual permeability value at a certain suction level as a fraction of its value at full saturation, i.e.

$$k(S) = k_{sat} \cdot k_{rel} \quad (18)$$

where  $k_{rel}$  can be calculated according to van Genuchten (1980) as

$$k_{rel} = \sqrt{S_e} [1 - (1 - S_e^{n_s/(n_s-1)})^{1-1/n_s}]^2 \quad (19)$$

where  $n_s$  is the fitting parameter used in Eq. (16). For the current analysis, the fitting parameters,  $\alpha_{sw}$  and  $n_s$ , were chosen to be 0.44 and 3.04, respectively, which are typical values for a sandy silt (Abed,

2008), and the corresponding van Genuchten curve is shown in Fig. 6. The other material properties needed for the slope collapse analysis are listed in Table 2. A high permeability was used to speed up the wetting part of the analysis for illustrative purposes, and due to the fixed pore pressure boundary the progression of the wetting front will be linearly affected; e.g. by reducing the permeability by a factor of 10, the wetting front will move 10 times slower. Note that large density changes may occur during large deformations, and that these are likely to cause changes in material properties, including the stiffness, shear strength and permeability. However, as the focus of this paper is to demonstrate the large strain and triggering behaviours of the model, these features have not been included.

### 3.2. Collapse process

The numerical simulation has two steps: (1) gravity loading to generate the in-situ stresses and the application of an initial prescribed suction of 50.0 kPa across the domain; and (2) a zero pore water

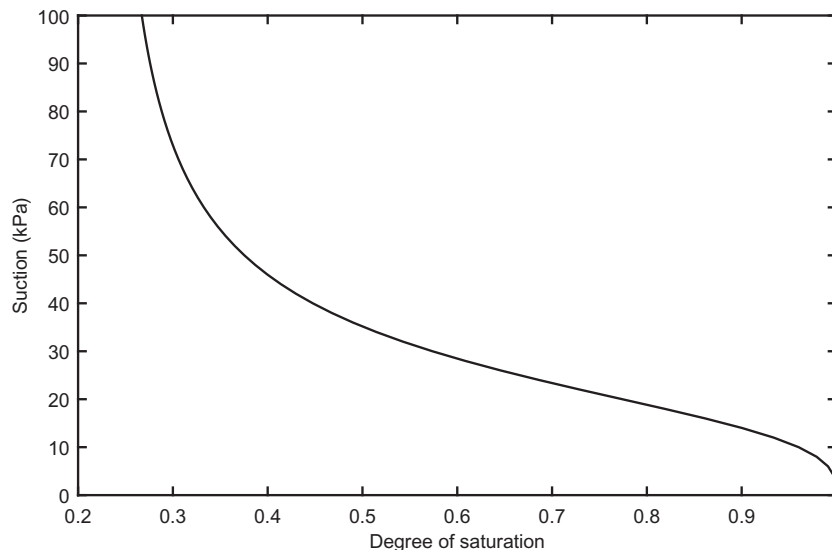


Fig. 6. Soil-water retention curve considered in the analysis.

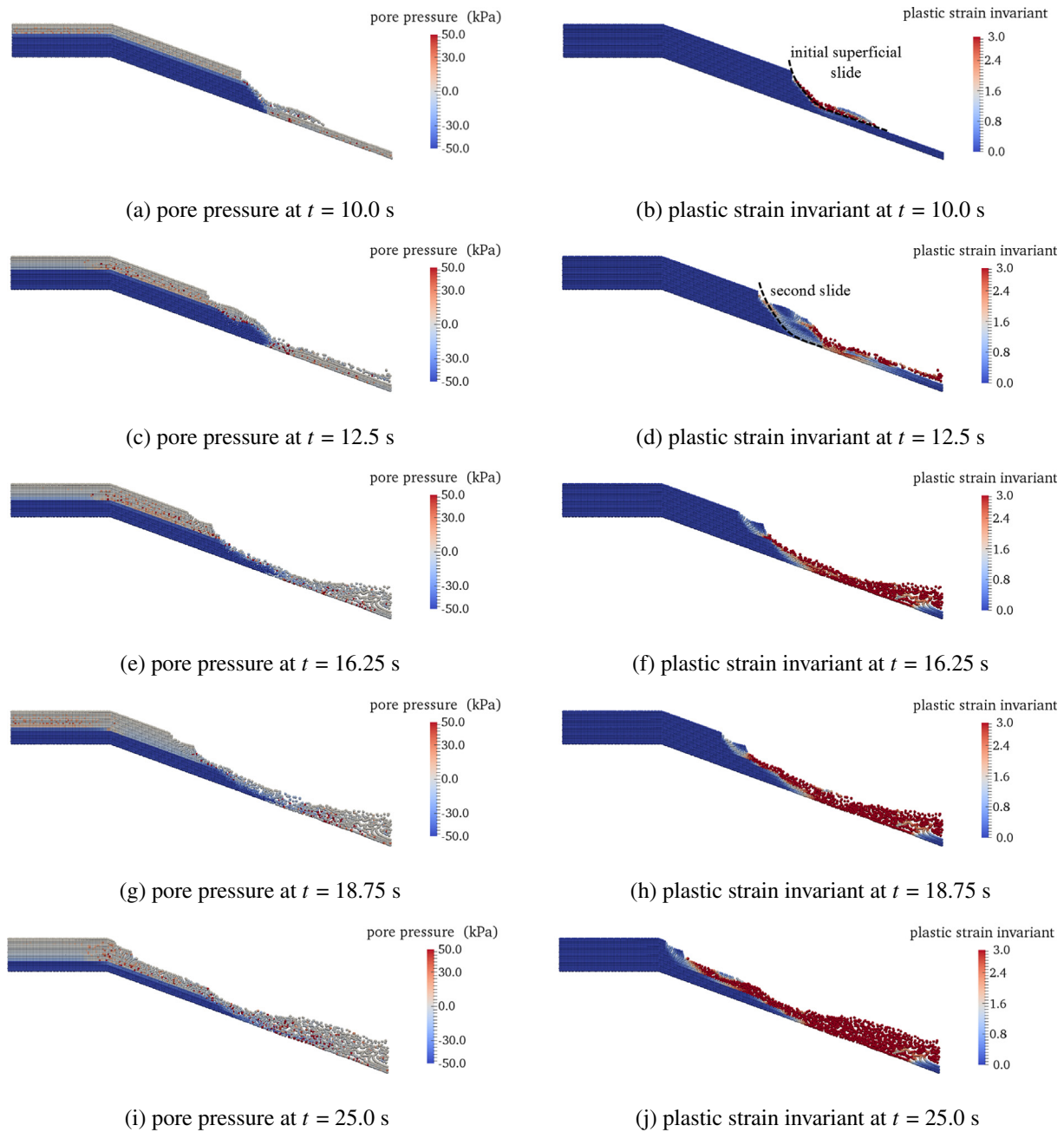


Fig. 7. Rainfall-induced slope collapse process in terms of pore pressure and plastic shear strain invariant contours.

pressure applied to the slope surface to model continuous water infiltration into the slope, until either a slope failure occurs or an equilibrium condition is reached.

For simplicity, the suction was initially assumed to be constant throughout the slope, whereas, for modelling the fully saturated soil at the boundary, zero pore pressure was applied to the material points located in the surface elements, to simulate a rainfall event providing the maximum inflow flux possible, and maintained throughout the simulation. The disadvantage of dealing with the boundary in this way is that it may cause some unrealistic outcomes, as some material points assigned a zero pore pressure may move a long distance and end up as non-boundary material points. This aspect will be the subject of a future investigation.

Fig. 7 shows the collapse process of the slope when subjected to rainfall infiltration, where the plastic shear strain invariant contours are shown on the right-hand-side of the figure, and the pore pressure

contours are shown on the left-hand-side, at five different times. The analysis used a time step size of  $5.0 \times 10^{-5}$  s to avoid non-convergence in the large deformation phase. Using an Intel Xeon E5–1620 processor, the analysis took approximately 3–4 h to execute on a single core.

In Fig. 7(a, b), i.e. at  $t = 10$  s, an initial failure occurs at the slope surface as this part of the slope becomes fully saturated, which implies an increase of the pore pressure and hence a decrease in the soil strength. As this small body of soil moves downslope, lateral support is removed from the soil upslope and the soil continues to saturate, and a wedge-shaped soil block forms through both the saturated and unsaturated parts (Fig. 7(c, d)). At  $t = 16.25$  s (Fig. 7(e, f)), the soils within the saturated zone in the upper part of the slope are seen to fail, giving an impression of superficial slope failures leading to larger slope failures. Due to the change in the slope geometry, retrogression within the slope cross-section is able to continue, as seen with a further failure initiating at  $t = 18.75$  s (Fig. 7(g, h)). Fig. 7(i, j) shows the situation at

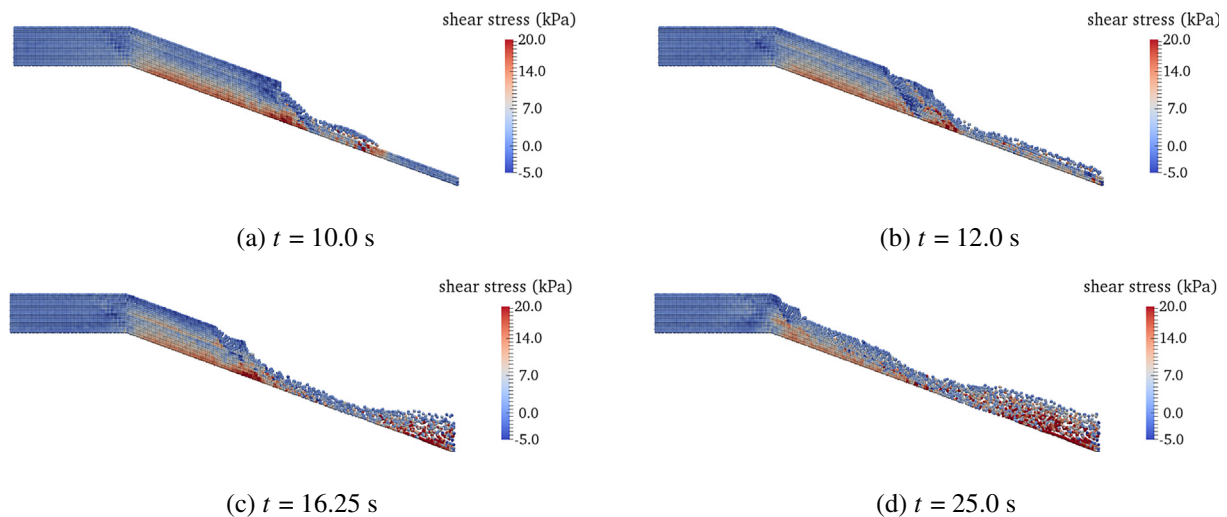


Fig. 8. Shear stress states at material points at different times.

$t = 25.0$  s, when a slope failure has developed throughout the full length of the slope, although initially made up of a series of individual failures. Note that the material ‘piles up’ against the right-hand boundary due to the prescribed size of the background mesh and the roller boundary condition, which have been included in the analysis to reduce the computation time.

The shear stress distributions within the slope at four distinct times are shown in Fig. 8. It is seen that the stress remains relatively unaffected in zones far from the failure planes. Moreover, the stresses are seen to be the largest on either side of the shear plane. The shear stresses within previous sliding soil blocks, when a new failure plane is forming, are shown to decrease. This may correspond to observations made for the single phase slope failure process (Wang et al., 2016b); i.e. these parts of the soil mass experience stress unloading, and are governed by the residual shear strength thereafter. Stress oscillations exist, and are mostly seen near the right-hand boundary, as in Fig. 8(c) and (d), and are thought to be mainly affected by the prescribed roller boundary condition, although integration at sub-optimal (non-Gaussian) points and the incompressibility of the soil in saturated conditions are also likely to have contributed to the oscillations seen in Fig. 8(a) and (b). Techniques such as the generalised interpolation material point (GIMP) method (Bardenhagen and Kober, 2004), integrations on the Gauss points (Beuth et al., 2011), and so on, can be utilised to combat the stress oscillations.

During the analysis, most of the failures are seen to be initiated in the saturated zone, with other failures being partly through the unsaturated zone. As the infiltration depth of the water becomes deeper, e.g. via an intense rainfall event, the failure depth of the soil is seen to increase. For example, in Fig. 7(a, b) a superficial slide near the steepest part of the slope is seen, as it becomes fully saturated. The second slide occurs further up the slope, again in the part of the slope that has become fully saturated (Fig. 7(c, d)). In this example, rainfall-induced progressive failure occurs partly because of the progressive loss of strength, but also due to the changing geometry, which, for example, may remove lateral support from the soil behind.

For most of the time considered in the analysis, the slope remains unsaturated at the base, so that the pore pressures in the saturated zone are maintained around zero. However, a limited positive pore pressure is just visible above the wetting front when the slope has been relatively undisturbed (stable) for a period of time, due to the higher permeability of the saturated soil, which can be observed most clearly in Fig. 7(a) and (g) at the top of the slope, in the horizontal section. At these times in the analysis only small failures are taking place and therefore only limited stress changes occur in the slope. Meanwhile, when a larger

failure occurs, positive pore pressures may be observed near the top of the slope, in the sloping section (as seen in Fig. 7(c), (e) and (i)), due to the shear stress relief (increase in mean stress) and contraction of the soil in the back scarp; at the same time negative pore pressures occur at the top of the slope, in the horizontal section, due to a reduction in the mean stress. It is noted that, due to the small number of elements (i.e. 2 in the depth direction) in the shallow, right-hand part of the slope and the prescription of zero pore pressure in the top two material points (initially in the top element), a lower than expected pore pressure is seen. Additionally, there are some oscillations in the positive pore pressures in the saturated zone. These may be partly caused by minor displacement errors, which can have an influence on the solution due to the compressible formulation of the water phase and the high bulk modulus of water.

The velocity of the water at material points initially just below the surface of the slope is presented in a non-dimensional form (velocity/hydraulic conductivity,  $v_w/K$ ) in Fig. 9. The initial positions of the points are indicated in Fig. 4, and the same points (i.e. solid material) are tracked through the analysis. All points are seen to have the same water velocity, which oscillates with a period of about 4 s. This oscillation is due to the mesh dependent behaviour of the flow in unsaturated conditions, for reasons including: (i) an increasing permeability as saturation increases (Eqs. (18) and (19)); and (ii) the relatively steep soil–water retention curve (Eq. 16). As can be seen in Fig. 7, these particular characteristics lead to fully saturated conditions above the water front and unsaturated conditions (with a pore pressure close to that of the initial conditions) immediately below. As the slope fails, the water velocity at each point in turn accelerates as the material containing that point accelerates. Point D, for example, fails in the second slide shown in Fig. 7(c, d), with the later velocity reversal occurring due to the material hitting the domain boundary, as seen in Fig. 7(g, h).

### 3.3. Comparison with total stress analysis

A total stress analysis has been undertaken for comparative purposes based on the same material parameters as above. Without any suction, the slope is initially unstable and the failure is triggered by gravity.

The progression of the slope failure at two different times is shown in Fig. 10. Fig. 10(a) shows two complete shear bands forming inside the slope at  $t = 0.5$  s; that is, a rotational slip in the down-slope part, and a translational slide over the whole slope length. The two shear bands are formed almost simultaneously and both failures reach the

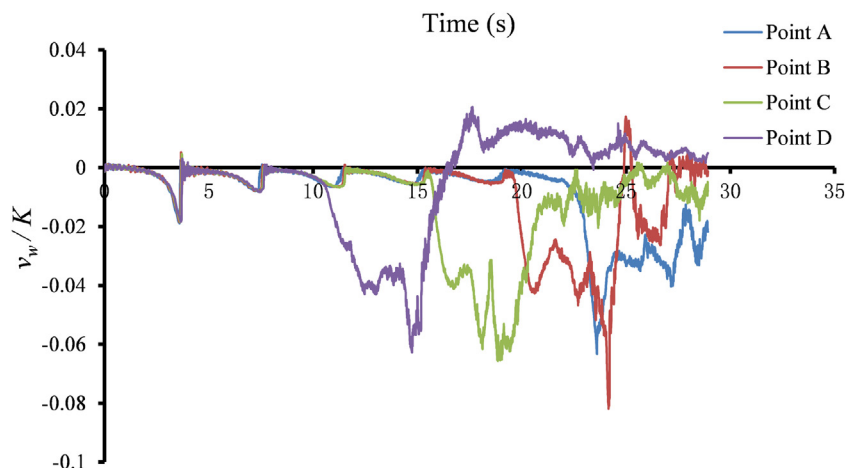


Fig. 9. Evolution of water velocity of material points A, B, C and D (see Fig. 4). Velocity expressed in non-dimensional form (velocity/hydraulic conductivity).

base of the soil layer. In contrast to the retrogressive failure caused by the slope geometry change seen in the rainfall-induced slope collapse, the slope failure here is mainly a translational failure of almost the entire slope. Fig. 10(b) shows the configuration of the deformed slope at time  $t = 2.0$  s, where it is seen that the soil body is mainly moving along the two shear bands.

Two things can be concluded, based on Fig. 10. Firstly, the slope experiences mainly a translational failure, in contrast to the rainfall-induced slope failure in Fig. 7 where retrogression occurs inside the slope. Secondly, the initial failure volume/area is much larger than for the (relatively more superficial) rainfall-induced slope failure.

### 3.4. Influence of soil friction angle

In this section, the influence of friction angle on the slope failure mechanism is discussed. Apart from the  $20^\circ$  case described above, friction angles of  $15^\circ$  and  $30^\circ$  have also been considered, with all other

material properties kept the same as in Table 2.

Fig. 11 shows the slope failure process when the friction angle equals  $30^\circ$ . As above, the plastic shear strain invariant contours are shown on the right-hand-side, and the pore pressure contours are shown on the left-hand-side. The failure initiates on the slope surface, when the surface soils become fully saturated, as shown in Fig. 11(a, b). Due to the lateral support removed from the upslope soils, and the continuing saturation of the soil, a series of retrogressive failures occur in the superficial zones of the slope. In contrast to the  $20^\circ$  case, failure only occurs inside the saturated zones, without propagating through the unsaturated zones, as shown in Fig. 11(c, d), due to the higher resistance arising from a higher friction angle. The retrogression appears to stop at a certain point, whereupon a big translational slide forms when the slope has become fully saturated, as illustrated in Fig. 11(e, f). Secondary failures are then seen to form within the moving mass, which resemble the failures observed under undrained conditions (Fig. 10).

For a friction angle of  $15^\circ$ , a different failure mode may be obtained

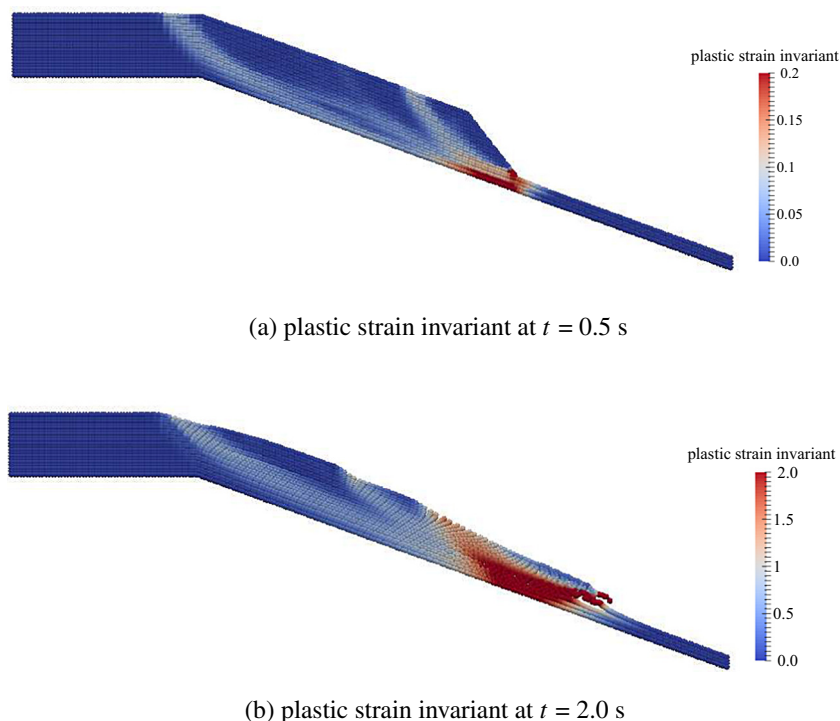


Fig. 10. Plastic shear strain invariant contours showing slope collapse using a total stress analysis.

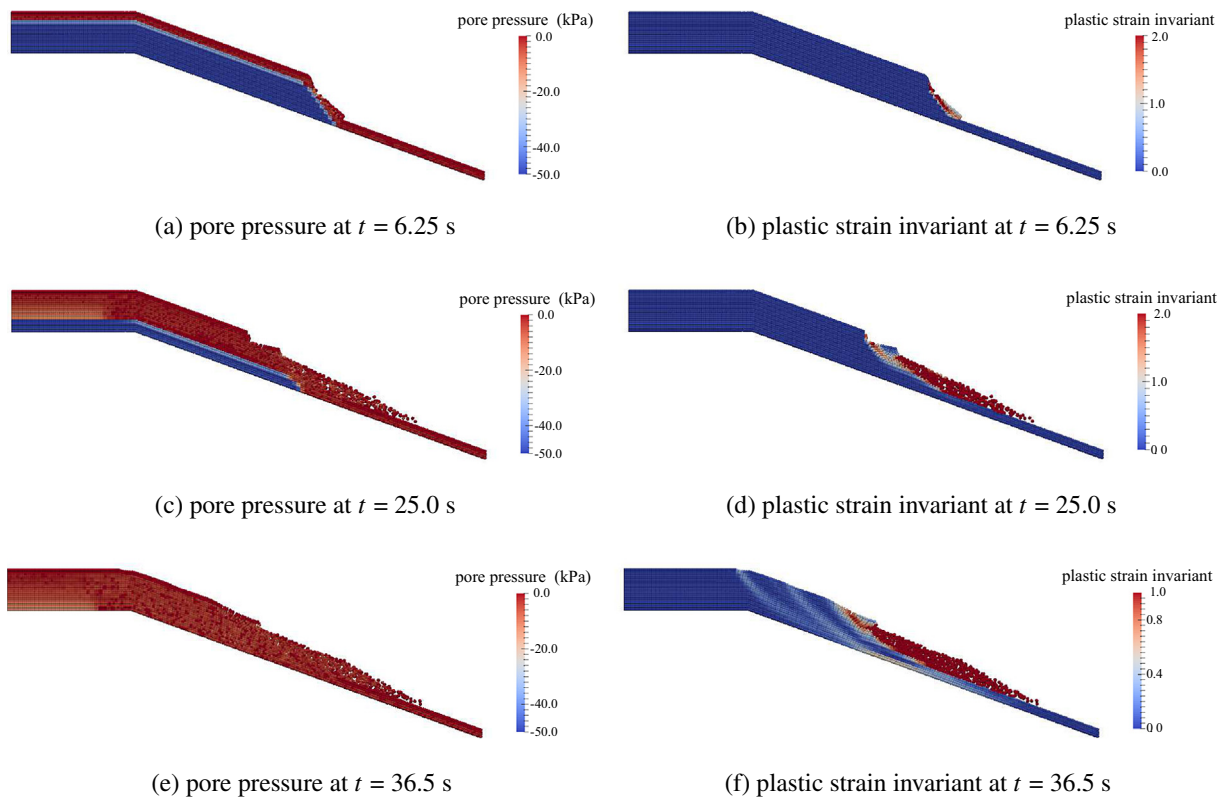


Fig. 11. Rainfall-induced slope collapse for friction angle equal to 30°.

as shown in Fig. 12. In Fig. 12(a, b), as the water starts to infiltrate into the soil, in contrast to the superficial failures in the saturated zones exhibited for the two larger friction angles, an initial circular failure plane forms in the downslope area. Strength loss is also expected along the failure surface, represented by the large plastic shear strain invariant contours. As part of the soils slide downslope, the whole slope failure is triggered, as indicated by a failure plane propagating down to the base of the soil layer along the entire length of the slope. The soil mass then dislocates into smaller volumes/areas, which results in the slope appearance having a step-like character, as seen in Fig. 12(c, d). Water is, however, only accumulated in very shallow zones due to the shorter time required for full failure to develop. Note that the slope was initially stable under gravity loading and the prescribed suction force.

To conclude, the soil friction angle is shown to have a significant impact on the slope failure mechanism. Most of the failures are seen to initiate and then retrogress backwards and upwards within the saturated zone during the infiltration process. As the friction angle increases, i.e. giving a higher soil resistance, the slope is more likely to experience a superficial failure constrained within the saturated zone. However, as the infiltration process continues, a whole slope collapse may be possible in a very similar manner to the undrained condition, leading to a big translational slide followed by a series of secondary failures. The retrogressive failures reported in clayey-type soils are seen to be possible as the friction angle decreases. This could be partly due to the sudden increase in soil weight as the surface soils become saturated.

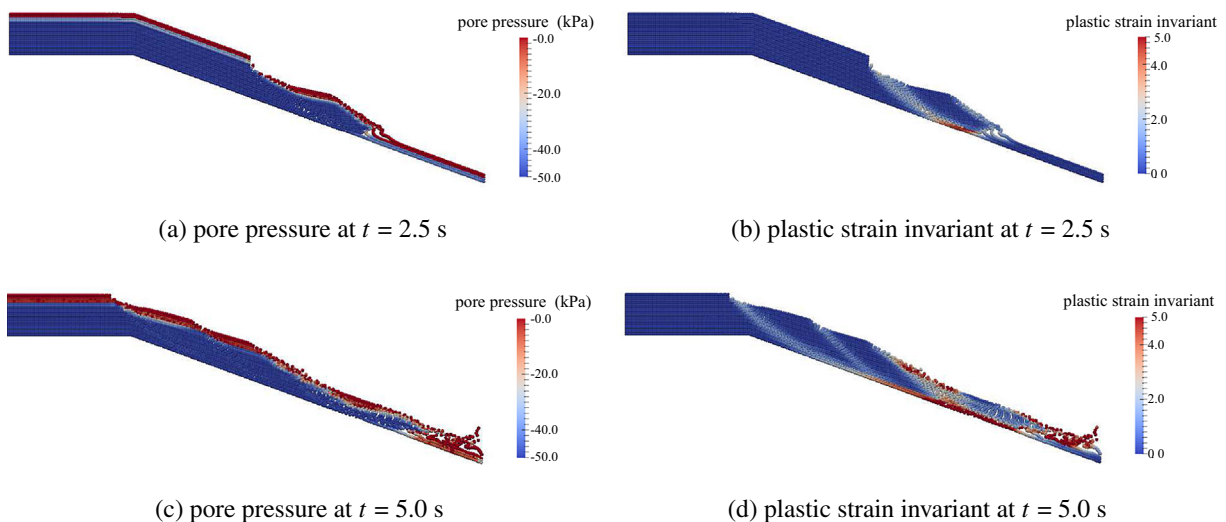


Fig. 12. Rainfall-induced slope collapse for friction angle equal to 15°.

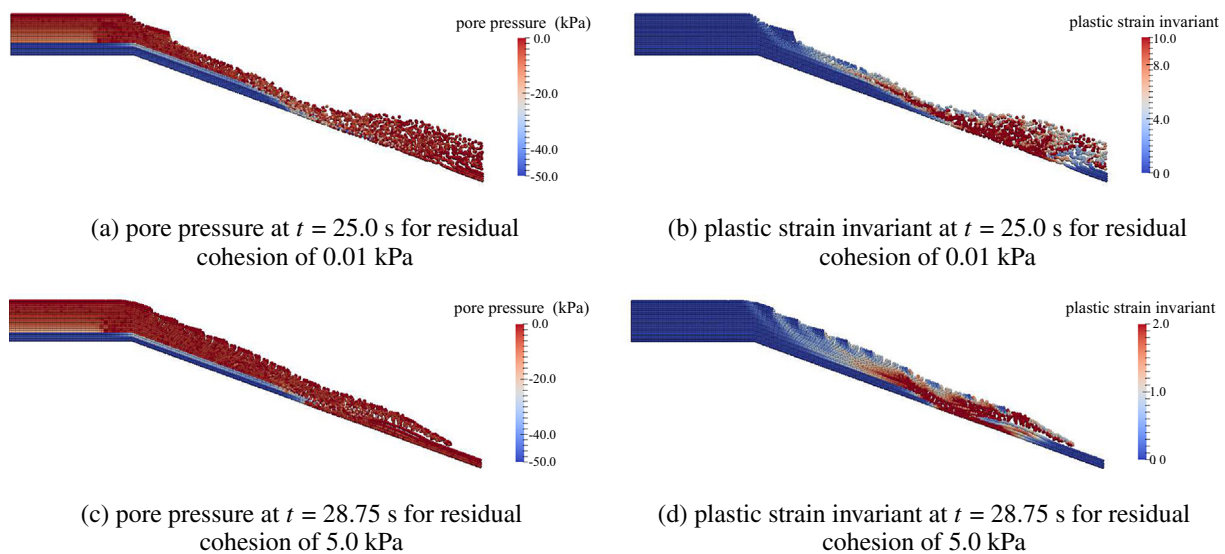


Fig. 13. Influence of residual cohesion on slope failure mechanism.

### 3.5. Influence of residual cohesion

Fig. 13 shows the final configurations of the slope collapse, when the failure is fully developed throughout the slope, for residual cohesions of 0.01 kPa and 5.0 kPa. Other material properties are the same as for the base case.

Fig. 13(a, b) shows the final slope configuration for a residual cohesion of 0.01 kPa, which shows very little difference to the base case; i.e. a steep rear scarp is normally completely exposed prior to the development of the next slide. As some soil slides away, the lateral support to the soils upslope is reduced, thereby initiating the next failure in the sequence. Fig. 13(c, d) shows the failure mechanism for the slope with a residual cohesion of 5.0 kPa. Note that the shallow slips have occurred successively in a retrogressive way, even without the rear scarp being completely exposed. It is different from the case illustrated in Fig. 11(f), where a big translational slide occurs first, followed by secondary failures that form within the moving mass. As stated in Thomson and Hayley (1975) and van Asch et al. (1984), a slight movement of the soil blocks can cause sufficient reductions of the lateral support to cause retrogressive failures.

The soil strength can be decomposed into the cohesive strength (i.e. bonding forces in between the soil grains) and the frictional strength. With a smaller residual cohesion, the cohesive strength can be almost completely removed, and the strength is then almost proportional to stress. In this case a diffuse failure occurs and no distinct back-scarp remains. With a higher residual cohesion, a steep rear scarp is left and the soils behind may become unstable and hence the next failure is initiated. As the cohesion increases, the cohesive strength of the soil lessens the sliding distance during the slope failures. This gives a failure pattern similar to that normally observed in clayey-type soils, as reported in van Asch et al. (1984).

## 4. Discussion

MPM and coupled hydro-mechanical MPM are new methods which are able to tackle failure initiation, through to failure development and a final quasi-static system. It has been seen in the analyses in this paper that MPM is able to simulate the strong effects of the hydro-mechanical state of the soil system during failure initiation and failure progression in time. The method is able to solve slope failure simulations without constraints such as pre-defining the failure shape and having restrictive fixed geometries. However, it is noted that the method still has a number of limitations and these are discussed non-exhaustively as follows.

The method is fundamentally a continuum method which has FEM at its heart; therefore, issues such as mesh sensitivity and discrete features, e.g. cracks or fractures, need special treatment. Stress oscillations occur in both the effective stresses and pore pressures; although there are a number of methods to tackle this, such as GIMP (Bardenhagen and Kober, 2004) and CPM (Gonzalez Acosta et al., 2017), none has yet managed to eliminate them. Boundary conditions that do not align well with the mesh are difficult to apply accurately, although recent work has begun to address this (Remmerswaal, 2017; Cortis et al., 2018). Finally, it is noted that compared to analytical methods and FEM, the computational effort is very high; therefore, it is considered a useful method to simulate the full failure, but not in determining an initial failure or factor of safety.

## 5. Conclusions

An initial investigation of a rainfall-induced slope failure with coupled MPM has been presented in this paper. The method has been able to simulate the slope failure from initiation through to the post-failure processes. A long slope on an inclined base has been analysed, and it has been shown that rainfall-induced failure may be characterised by a series of mainly superficial failures, as are often observed in practice. This retrogressive failure mode is very different from that obtained in a total stress analysis, where a large translational slide is obtained for the slope geometry considered.

Parametric studies regarding friction angles and residual cohesion have been conducted. With a higher friction angle, the slope may fail due to a large translational slide during an intensive rainfall event (making the slope saturated within a short time), without showing retrogression during the infiltration process. As the friction angle decreases, the retrogression is more obviously seen, through both saturated and unsaturated zones. As for the influence of the residual cohesion, it is shown that, when a higher residual cohesion is assigned, shallow successive slips are exhibited without the complete exposure of the rear scarp during the failure process. In contrast, a smaller cohesion may lead to steeper rear scarps being exposed. It is thought that the coupled MPM, with further development, can be utilised to investigate a wide range of slopes at risk of rainfall-induced failure, including those susceptible to multiple and progressive failures.

## Acknowledgments

The authors wish to acknowledge the Funds for Creative Research

Groups of China (Grant No. 51621006), the China Scholarship Council, the Geo-Engineering Section of Delft University of Technology, the Netherlands and the “100 Talents” Program of the Chinese Academy of Sciences for their financial support of the first author.

## References

- Abe, K., Soga, K., Bandara, S., 2013. Material point method for coupled hydromechanical problems. *J. Geotech. Geoenviron.* 140 (3), 1–16.
- Abed, A., 2008. Numerical Modeling of Expansive Soil Behavior. In: Stuttgart University, (Ph.D. Thesis).
- Bandara, S., Soga, K., 2015. Coupling of soil deformation and pore fluid flow using material point method. *Comput. Geotech.* 63, 199–214.
- Bardenhagen, S.G., Kober, E.M., 2004. The generalised interpolation material point method. *Comput. Model. Eng. Sci.* 5 (6), 477–495.
- Beuth, L., Wieckowski, Z., Vermeer, P.A., 2011. Solution of quasi-static large-strain problems by the material point method. *Int. J. Numer. Anal. Methods Geomech.* 35 (13), 1451–1465.
- Borja, R.I., White, J.A., Liu, X.Y., Wu, W., 2012. Factor of safety in a partially saturated slope inferred from hydro-mechanical continuum modeling. *Int. J. Numer. Anal. Methods Geomech.* 36 (10), 223–248.
- Brand, E.W., 1981. Some thoughts on rain-induced slope failures. In: Proceedings of the 10th International Conference on Soil Mechanics and Foundation Engineering Vol. 3. Stockholm, Sweden, pp. 373–376.
- Cai, F., Ugai, K., 2004. Numerical analysis of rainfall effects on slope stability. *Int. J. Geomech.* 4 (2), 69–78.
- Cascini, L., Cuomo, S., Pastor, M., Sorbino, G., 2009. Modeling of rainfall-induced shallow landslides of the flow-type. *J. Geotech. Geoenviron.* 136 (1), 85–98.
- Chen, Z., Brannon, R., 2002. An evaluation of the material point method. In: Report SAND2002-0482. Sandia National Laboratories.
- Cortis, M., Coombs, W., Augarde, C., Brown, M., Brennan, A., Robinson, S., 2018. Imposition of essential boundary conditions in the material point method. *Int. J. Numer. Methods Eng.* 113 (1), 130–152.
- Dai, F.C., Lee, C.F., 2001. Frequency–volume relation and prediction of rainfall-induced landslides. *Eng. Geol.* 59 (3–4), 253–266.
- Fredlund, D.G., Rahardjo, H., 1993. *Soil Mechanics for Unsaturated Soils*. John Wiley and Sons, New Jersey.
- Gonzalez Acosta, L., Vardon, P.J., Hicks, M.A., 2017. Compound material point method (CMPM) to improve stress recovery for quasi-static problems. *Procedia Eng.* 175, 324–331.
- Hughes, T.J., 1980. Generalization of selective integration procedures to anisotropic and nonlinear media. *Int. J. Numer. Methods Eng.* 15 (9), 1413–1418.
- Hungr, O., 2003. Flow slides and flows in granular soils. In: Proceedings of the International Workshop on Flows – Occurrence and Mechanisms of Flows in Natural Slopes and Earthfill. Sorrento, Italy, pp. 37–44.
- Jassim, I., Stolle, D., Vermeer, P.A., 2013. Two-phase dynamic analysis by material point method. *Int. J. Numer. Anal. Methods Geomech.* 37 (15), 2502–2522.
- Kularathna, S., Soga, K., 2017. Projection method in material point method for modeling incompressible materials. *Procedia Eng.* 175, 57–64.
- Leroueil, S., 2001. Natural slopes and cuts: movement and failure mechanisms. *Géotechnique* 51 (3), 197–243.
- Lewis, R.W., Schrefler, B.A., 1998. *The Finite Element Method in the Static and Dynamic Deformation and Consolidation of Porous Media*, 2nd Edition. John Wiley and Sons, Chichester.
- Liakopoulos, A.C., 1964. *Transient Flow through Unsaturated Porous Media*. University of California, Berkeley (Ph.D. Thesis).
- Lim, L.J., Andreykiv, A., Brinkgreve, R.B.J., 2014. On the application of the material point method for offshore foundations. In: Proceedings of the 8th European Conference on Numerical Methods in Geotechnical Engineering vol. 1. Delft, the Netherlands, pp. 253–258.
- Lin, C.W., Liu, S.H., Lee, S.Y., Liu, C.C., 2006. Impacts of the Chi-Chi earthquake on subsequent rainfall-induced landslides in central Taiwan. *Eng. Geol.* 86 (2–3), 87–101.
- Maljaars, J., Labeur, R.J., Möller, M., Uijtewaald, W., 2017. A numerical wave tank using a hybrid particle-mesh approach. *Procedia Eng.* 175, 21–28.
- Pastor, M., Fernandes Merodo, J.A., Gonzalez, E., Mira, P., Li, T., Liu, X., 2004. *Modelling of Landslides: (I) Failure Mechanisms*. Springer.
- Rahardjo, H., Ong, T.H., Rezaur, R.B., Leong, E.C., 2007. Factors controlling instability of homogeneous soil slopes under rainfall. *J. Geotech. Geoenviron.* 133 (12), 1532–1543.
- Remmerswaal, G., 2017. *Development and Implementation of Moving Boundary Conditions in the Material Point Method*. Delft University of Technology (M.Sc. Thesis).
- Soga, K., Alonso, E.E., Yerro, A., Kumar, K., Bandara, S., 2016. Trends in large-deformation analysis of landslide mass movements with particular emphasis on the material point method. *Géotechnique* 66 (3), 248–273.
- Sulsky, D., Chen, Z., Schreyer, H.L., 1994. A particle method for history-dependent materials. *Comput. Methods Appl. Mech. Eng.* 118 (1–2), 179–196.
- Sulsky, D., Zhou, S., Schreyer, H.L., 1995. Application of a particle-in-cell method to solid mechanics. *Comput. Phys. Commun.* 87 (1), 236–252.
- Thomson, S., Hayley, D.W., 1975. The Little Smoky Landslide. *Can. Geotech. J.* 12 (3), 379–392.
- Tsaparas, I., Rahardjo, H., Toll, D.G., Leong, E.C., 2002. Controlling parameters for rainfall-induced landslides. *Comput. Geotech.* 29 (1), 1–27.
- USGS, 2004. *Landslide Types and Processes*. In: Fact Sheet 2004-3072. USGS.
- Van Asch, T., Brinkhorst, W., Buist, H., Vessem, P., 1984. The development of landslides by retrogressive failure in varved clays. *Z. Geomorph. NF. Suppl. Bd.* 4, 165–181.
- Van Esch, J., Stolle, D., Jassim, I., 2011. Finite element method for coupled dynamic flow deformation simulation. In: Proceedings of the 2nd International Symposium on Computational Geomechanics. Dubrovnik, Croatia, pp. 415–424.
- Van Genuchten, M.T., 1980. A closed-form equation for predicting the hydraulic conductivity of unsaturated soils. *Soil Sci. Soc. Am. J.* 44 (4), 892–898.
- Vardon, P.J., 2015. Climatic influence on geotechnical infrastructure: a review. *Environ. Geotech.* 2 (3), 166–174.
- Verruijt, A., 2009. *An Introduction to Soil Dynamics*. Springer Science and Business Media.
- Wang, B., Vardon, P.J., Hicks, M.A., Chen, Z., 2016a. Development of an implicit material point method for geotechnical applications. *Comput. Geotech.* 71, 159–167.
- Wang, B., Vardon, P.J., Hicks, M.A., 2016b. Investigation of retrogressive and progressive slope failure mechanisms using the material point method. *Comput. Geotech.* 78, 88–98.
- Wang, B., Hicks, M.A., Vardon, P.J., 2016c. Slope failure analyses using the random material point method. *Géotech. Lett.* 6 (2), 113–118.
- Wu, L.Z., Selvadurai, A.P.S., Zhang, L.M., Huang, R.Q., Huang, J., 2016. Poro-mechanical coupling influences on potential for rainfall-induced shallow landslides in unsaturated soils. *Ad. Wat. Res.* 98, 114–121.
- Yerro, A., Alonso, E.E., Pinyol, N.M., 2015. The material point method for unsaturated soils. *Géotechnique* 65 (3), 201–217.
- Zabala, F., Alonso, E.E., 2011. Progressive failure of Aznalcollar dam using the material point method. *Géotechnique* 61 (9), 795–808.
- Zhang, H.W., Wang, K.P., Zhang, Z., 2007. Material point method for numerical simulation of failure phenomena in multiphase porous media. In: Proceedings of the International Symposium on Computational Mechanics. Beijing, China, pp. 36–47.
- Zhang, H.W., Wang, K.P., Chen, Z., 2009. Material point method for dynamic analysis of saturated porous media under external contact/impact of solid bodies. *Comput. Methods Appl. Mech. Eng.* 198 (17–20), 1456–1472.
- Zienkiewicz, O.C., Chang, C.T., Bettess, P., 1980. Drained, undrained, consolidating and dynamic behaviour assumptions in soils. *Géotechnique* 30 (4), 385–395.